


Trapping and self-assembly of particles by photonic chiral surface wavesLiyong Cui ^{1,2} and Neng Wang^{1,*}¹*Institute of Microscale Optoelectronics, Shenzhen University, Shenzhen 518060, China*²*Hunan Provincial Laboratory of Flexible Electronic Materials Genome Engineering, Changsha University of Science and Technology, Changsha 410014, China*

(Received 11 January 2022; revised 2 April 2022; accepted 3 May 2022; published 16 May 2022)

Trapping and self-assembly of particles by a single photonic chiral surface wave (PCSW) in a waveguide is investigated in this work. Through rigorous calculations, stability analysis, and physical interpretation using response theory of optical force, we show that particles of arbitrary sizes, shapes, and dielectric constants can be stably trapped and assembled in the waveguide which is counterintuitive since a propagating surface wave usually exerts a pushing or pulling force on the particle and transports it. The ability of confinement is due to that the PCSW can navigate the particle and recover to its original state. Because of the unique propagating and scattering properties, there is no interaction among the particles when the particles are far away enough. Thus, the particles are independently trapped during the self-assembly process. This work provides a different approach to manipulate small particles by using the PCSW.

DOI: [10.1103/PhysRevA.105.053512](https://doi.org/10.1103/PhysRevA.105.053512)**I. INTRODUCTION**

Optical trapping—the localization and manipulation of microscopic particles by light [1–3], has advantages of noncontact and noninvasive manipulation at the proper wavelength and hence has been intensely exploited in various scientific areas including atomic physics [4–6], biological science [7–9], Raman spectroscopy [10], and quantum physics [11]. Relying on the optical gradient force due to the inhomogeneity of light intensity, a single tightly focused laser beam can trap microscopic particles, which is well known as the optical tweezers [1–3]. Ingenious ways were invented to shape the laser beam to achieve novel functionalities [12].

In addition to conventional laser beams that propagate in free space, the localized surface plasmons [13–16] and surface waves including evanescent waves [17–20], surface plasmon polaritons [21–23], and Bloch surface waves [24,25] have been used for manipulating particles in the past decade. Owing to the enhanced electromagnetic intensity and intensity gradient near the interfaces, the localized surface plasmons are able to trap microscale and even nanoscale particles [26–29]. On the other hand, the flexibility on controlling the scattering of surface waves enables the surface waves to pull [30–34] and push [35] particles, offering a different paradigm in optomechanics [14,35–37]. At present, optical manipulations by surface waves are mainly focused on a single particle. When there is a collection of particles, optical binding [38–41] that is due to the multiple scattering among particles must be taken into account.

Recently, a novel type of surface wave—the photonic chiral surface wave (PCSW) which is supported on the interface between the photonic Chern insulator and topologically trivial material, has been proposed and widely studied. The PCSW

propagates unidirectionally and can continuously navigate around obstacles and restore to its original states due to the topological protection [42,43]. With the intriguing transporting and scattering properties, the PCSW has been applied in optical manipulations with unique properties. For example, by using the PCSW, an optical pulling scheme that is robust against the shapes, sizes, and permittivity of particles and even sharp corners can be achieved [36].

Instead of studying the transportation ability of the PCSW, in this work, we focused on the use of PCSW for optical trapping of particles. The PCSW we considered is supported in an air waveguide sandwiched between a magneto-optical photonic crystal (PC) which acts as a Chern insulator and an ordinary PC. The two PCs possess the same lattice constant; hence, the waveguide preserves discrete translational symmetry. We found that within a lattice constant along the waveguide direction, the particle with small scattering cross section can be stably trapped to one or two positions which are located on the high-symmetry lines (edge and center) of the supercell. When the scattering cross section of the particle is too large, it is stably trapped with the help of both the optical force and restriction of the waveguide boundary. Owing to the novel transporting and scattering properties of the PCSW, multiple particles can be individually trapped without the optical binding force, enabling the self-assembly of particles in the waveguide.

The paper is organized as follows: first, the waveguide supporting the chiral surface wave is introduced. Then, the equilibrium position of a single particle inside the waveguide is searched accompanied by the stability analysis. Response theory of optical force (RTOF) [44,45] is used to interpret the numerical results. Then, the self-assembly of two and three cylinders is studied. Then, the trapping of cylinders with square and equilateral triangular shapes is discussed briefly. Photophoretic forces are also discussed. Finally, a summary is given.

*nwang17@szu.edu.cn

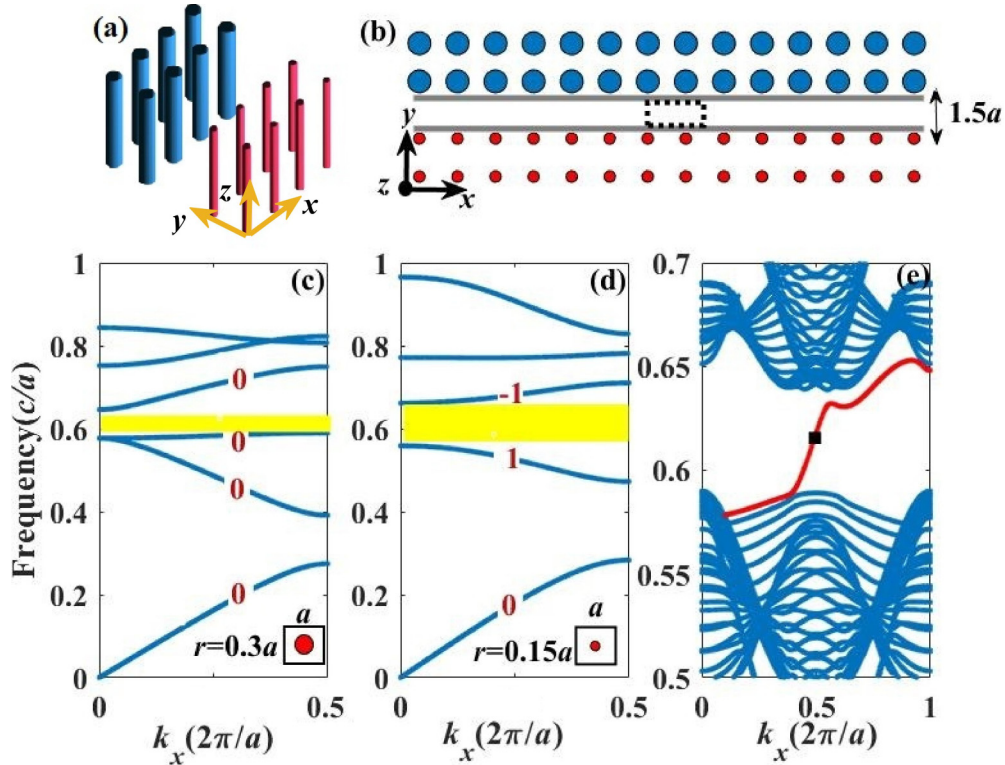


FIG. 1. (a), (b) Stereogram schematic and top view of the waveguide that supports a chiral surface mode. The waveguide is formed by an air gap sandwiched between a magneto-optical PC (red) and an ordinary PC (blue). The lattice constants of both PCs are a , and the ambient is air. The gray lines denote two thin barriers to prevent the particles from entering into the PCs, the cylinders are infinite along z direction. (c), (d) Band diagrams of the two PCs for TM polarization. The band gap between the third and fourth bands of the ordinary PC and the band gap between the second and third bands of the magneto-optical PC are shaded in yellow, and the Chern numbers of the bands near the band gaps are indicated. (e) Projection bands (blue) of the PCs and the surface band (red) at the interface (the lower is the magneto-optical PC) between the two PCs. The black dot denotes the chiral surface mode that is excited.

II. RESULTS AND DISCUSSION

A. The waveguide supporting the photonic chiral surface wave

The waveguide supporting a single photonic chiral surface mode is schematically shown in Figs. 1(a) (stereogram) and 1(b) [top view of (a)], where an air gap along the x direction is sandwiched between a magneto-optical PC (red disks) and an ordinary PC (blue disks). The two PCs are further separated by $0.5a$, where a is the lattice constant of both PCs. So, the center-to-center distance between the bottom cylinders of the upper PC and the top cylinders of the lower PC is $1.5a$. The radii of the cylinders of the magneto-optical PC and the ordinary PC are $0.15a$ and $0.3a$, respectively. Two extremely thin polytetrafluoroethylene ($\epsilon_r = 2.1$) plates (marked by the gray lines) are placed at the top and bottom of the air gap, respectively, to prevent the particles inside the waveguide from entering into the PCs. For the ordinary PC, the relative permittivity and permeability of the cylinders are $\epsilon_r=5.5$, $\mu_r=1.0$. For the magneto-optical PC, the relative permittivity of the cylinder is $\epsilon_r=12.5$, and the relative permeability tensor is

$$\mu_r = \begin{pmatrix} 1 & -0.4i & 0 \\ 0.4i & 1 & 0 \\ 0 & 0 & 1 \end{pmatrix}. \quad (1)$$

The most commonly used magneto-optical material is yttrium-iron-garnet (YIG), of which the permeability tensor can be tuned by adjusting the biased magnetic field [46]. However, the operation frequency of YIG is usually limited to the microwave regime. For higher-frequency domain, we can use composite materials with the magneto-optical effect enhanced by surface plasmon resonance [47–49]. Recently, Banthí *et al.* [50] experimentally realized simultaneous large magneto-optical effect and low optical losses using the Au/Co/Au magnetoplasmonic nanodisks with SiO₂ dielectric layer inserted properly at the optical frequency domain.

The band diagrams of the two PCs for TM (E_z) polarization are plotted in Figs. 1(c) and 1(d), respectively. As we can see, the second band gaps (shaded in yellow) of the two PCs overlap. The operating frequency of the waveguide will be in this overlapping range. Also, the Chern numbers of the bands near the two band gaps are calculated and indicated in the figure. For the ordinary PCs which possess time-reversal symmetry, all the bands are topologically trivial, namely their Chern numbers are zeros. But, for the magneto-optical PC, since the band gap is formed due to the lifting of degeneracy between the second and third bands at the Γ point induced by time-reversal symmetry breaking, the bands above and below the band gap become topologically nontrivial.

By summing up the Chern numbers of all bands below the band gap, we obtained that the gap-Chern number of

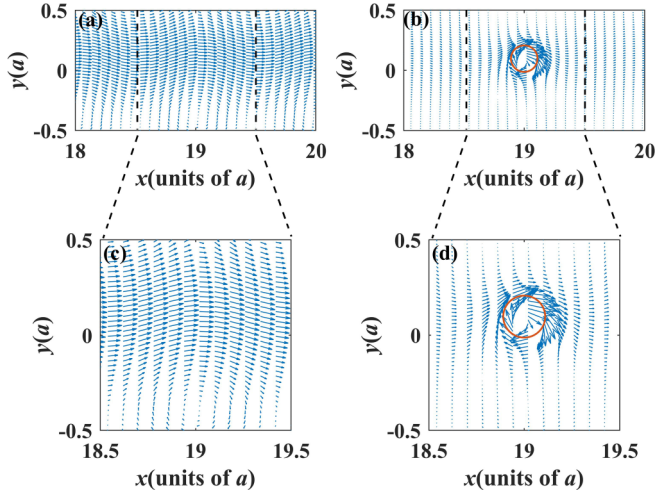


FIG. 2. The Poynting vectors of a PCSW propagating in the waveguide without (a) and with (b) a particle located in the waveguide. The radius and refractive index of the particle are $r = 0.15a$ and $n = 4.0$, respectively. The location of the particle is $x = 19a$ and $y = 0.0973a$. (c), (d) Enlarged view of the rectangle areas in (a) and (b), respectively.

the ordinary PC is zero, while the gap-Chern number of the magneto-optical PC is 1. Therefore, according to the bulk-boundary correspondence [51], there will be a chiral surface mode with the positive group velocity (propagating along the positive- x direction) on the interface formed by the upper ordinary PC and the lower magneto-optical PC. In Fig. 1(e), the projections of the bulk bands (blue lines) of the two PCs and the surface band (red line) on the interface by a supercell calculation are shown. As expected, there is one gapless surface state with the positive group velocity. In the waveguide, the PCSW is excited at a given frequency $\omega = 0.618c/a$ [marked by the black dot in Fig. 1(e)] by a line current source located in the waveguide. Throughout this paper, the current source is 0.01A. Figures 2(a) and 2(b) show the Poynting vectors of a PCSW propagating in the waveguide without [Fig. 2(a)] and with a particle [Fig. 2(b)] located in the waveguide. The radius and refractive index of the cylinder are $r = 0.15a$, and $n = 4.0$, respectively. The location of the cylinder is $x = 19a$ and $y = 0.0973a$. Figures 2(c) and 2(d) are the zoomed view of the rectangle areas in Figs. 2(a) and 2(b), respectively. As can be seen from Figs. 2(b) and 2(d), there is no leftward energy flux when away from the cylinder and the energy fluxes recover themselves about half lattice period downstream from the cylinder. Therefore, the PCSW can navigate the particle and propagate forward without reflection. In the following, we will show that this PCSW can trap and self-assemble multiple cylinders inside the waveguide.

B. Stable trapping of cylinders

We have performed full-wave simulations with commercial software COMSOL MULTIPHYSICS and applied the Maxwell stress tensor (MST) to calculate the optical force [52]. For a time-harmonic wave, the time-averaged optical force on a particle located in air is rigorously calculated by an integral of

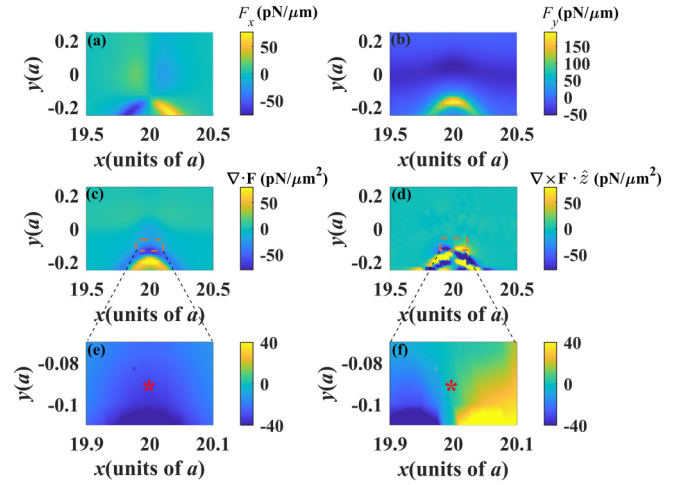


FIG. 3. Longitudinal (a) and transversal (b) optical forces acting on the dielectric cylinder as a function of its location (x, y) within a rectangular region as marked by the black dotted rectangle in Fig. 1(b). The radius and refractive index of the cylinder are $r = 0.15a$ and $n = 2$, respectively. (c), (d) Divergence and curl of the optical force. (e), (f) Zoomed view of the rectangular area in (c) and (d), respectively. The stars denote the equilibrium position.

the MST over a closed surface enclosing the particle:

$$\mathbf{F} = \oint_S \vec{\mathbf{T}} \cdot \mathbf{n} dS, \quad (2)$$

where S is the closed surface immersed in air, \mathbf{n} is the outward normal unit vector of S , and dS is the differential element of the surface. $\vec{\mathbf{T}}$ is the MST given by

$$\vec{\mathbf{T}} = \frac{1}{2} \varepsilon_0 \left[\mathbf{E} \mathbf{E}^* + c^2 \mathbf{B} \mathbf{B}^* - \frac{1}{2} (\mathbf{E} \cdot \mathbf{E}^*) \mathbf{I} - \frac{c^2}{2} (\mathbf{B} \cdot \mathbf{B}^*) \mathbf{I} \right], \quad (3)$$

where \mathbf{E} and \mathbf{B} are the electric and magnetic fields, respectively, ε_0 is the permittivity of the free space, c is the light speed in vacuum, \mathbf{I} is the 3×3 identity matrix, and $*$ denotes taking the complex conjugate. The particle we consider is a cylinder which is infinitely long along the z direction. Based on Eq. (2), the longitudinal (x direction) and the transversal (y direction) optical forces on a dielectric cylinder with the radius $r = 0.15a$ and the refractive index $n = 2.0$ as function of its locations (x, y) within a rectangular region [marked by the dotted rectangle in Fig. 1(b)] are calculated and shown in Figs. 3(a) and 3(b), respectively. This rectangular region basically covers all the positions that the particle can reach along the y direction. Note that the x coordinates of the cylinders of the PCs are Na , where N is an integer, and the central line of the air gap is at $y = 0$. Because there is no mirror symmetry with respect to $y = 0$, the chiral surface mode is neither even nor odd, and the transversal optical force is not necessarily zero at $y = 0$. Thus, we have to seek equilibriums along the y direction. From Fig. 3, we see that the optical force repeats itself when the particle moves a lattice constant along the x direction. This is expected because the waveguide preserves discrete translational symmetry along the x direction. Another key point is that the longitudinal optical force is always zero when the particle is located at

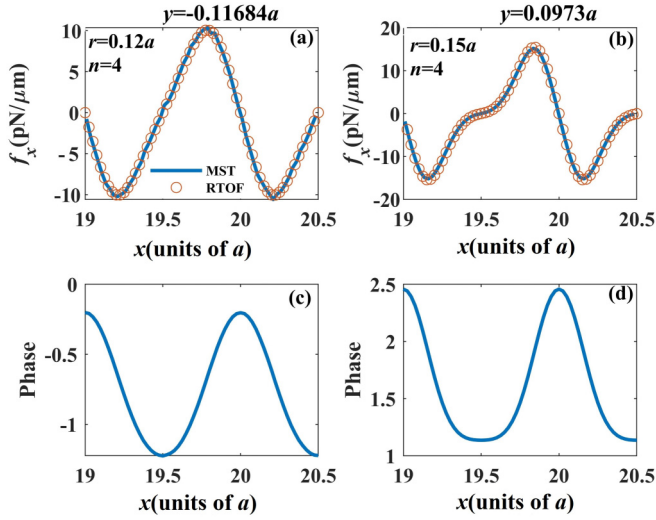


FIG. 4. (a), (b) Optical forces calculated by using the MST (blue solid line) and RTOF (red circles) along an axial segment. The y coordinates of the cylinders in (a) and (b) are fixed at $y = -0.11684a$ and $y = 0.0973a$, respectively. The radii and refractive indices of the cylinders are (a) $r = 0.12a$, $n = 4$ and (b) $r = 0.15a$, $n = 4$, respectively. (c), (d) Phase responses corresponding to (a) and (b), respectively.

$x = Na$ and $x = (N + 1/2)a$, irrespective of its transversal location, which can be interpreted by the RTOF [44,45].

RTOF is proposed by Rakich *et al.* based on the virtual work principle in the adiabatic limit [44,45]. It provides a powerful tool to analyze the optical force in multiport photonic systems. Because the waveguide supports only one mode [see Fig. 1(e)], there will be no mode conversion. According to

RTOF, the optical force acting on the particle can be calculated by

$$\mathbf{F}(x, y) = \frac{I(x, y)}{\omega} \nabla \phi(x, y), \quad (4)$$

where ω is the angular frequency of light, I and ϕ are the power and the phase response with respect to the location of the particle. The power and the phase response can be evaluated from the complex amplitude of the scattered mode defined as

$$E = \frac{1}{2} v_g \epsilon_0 \epsilon_r \int E_{zeig} E_z^* dS, \quad (5)$$

where E_{zeig} is the electric field distribution of the eigenmode [see its real part, shown in Figs. 5(e) and 5(f)] by the supercell calculation, E_z is the electric field distribution inside a unit supercell at a fixed location downstream from the particle, and $v_g = d\omega/dk$ denotes the group velocity of the chiral surface mode. The power and phase response are then calculated according to

$$I = |E|^2, \quad \phi = \text{Arg}(E). \quad (6)$$

Due to discrete translational symmetry of the waveguide, both I and ϕ restore their initial values when the particle moves a lattice constant along the x direction. As a result, $\partial\phi(x, y)/\partial x$ oscillates between positive and negative, and the longitudinal equilibrium ($F_x = 0$) occurs when $\partial\phi(x, y)/\partial x = 0$. It has been shown that $\phi(x, y)$ has even symmetry with respect to high-symmetry lines $x = Na$ and $x = (N + 1/2)a$ when the particle is symmetric (round shape for example) [53] (see the Appendix). Therefore, $\partial\phi(Na, y)/\partial x = \partial\phi(Na + a/2, y)/\partial x = 0$, leading to

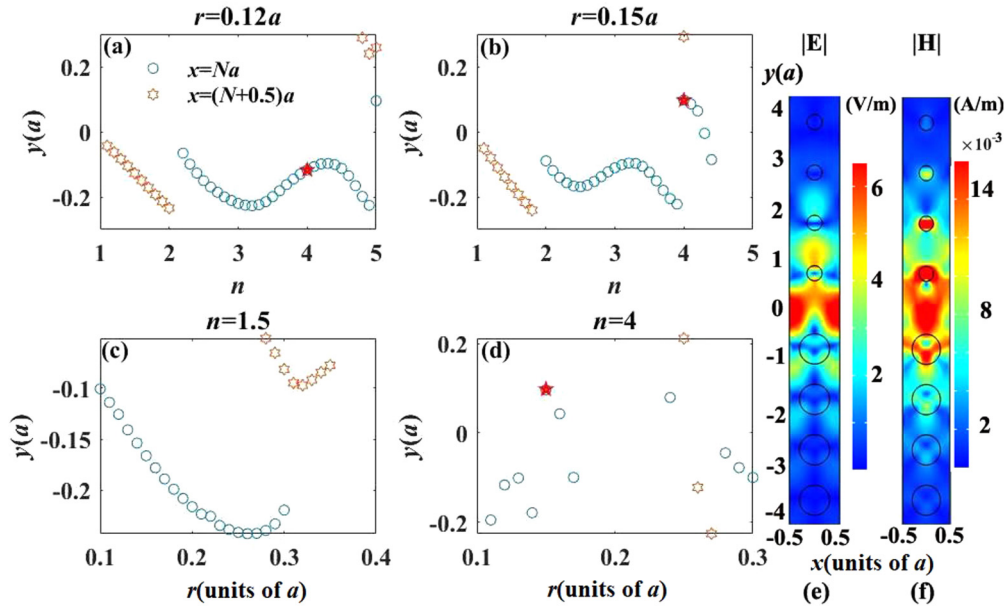


FIG. 5. Equilibrium positions of the cylinder as functions of its refractive index [(a) and (b)] and its radius [(c) and (d)]. The blue circles denote that the cylinder is trapped at the position $x = Na$, while the orange hexagons represent that the cylinder is trapped at the position $x = (N + 0.5)a$, where N is an integer. The radii in (a) and (b) are $r = 0.12a$ and $r = 0.15a$, respectively, and the refractive indexes in (c) and (d) are $n = 1.5$ and $n = 4.0$, respectively. The red stars in (a) and (b) denotes the y coordinates used in Figs. 3(a) and 3(b), respectively. The red stars in (b) and (d) are for the same particle. (e), (f) Distribution of electric fields and magnetic fields.

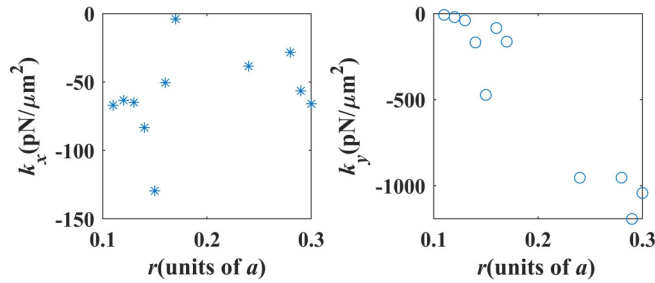


FIG. 6. Eigenvalues of the force constant matrices of the equilibrium positions in Fig. 5(d).

the vanishment of longitudinal optical force at the high-symmetry lines of the supercell $x = Na$ and $x = (N + 1/2)a$.

To show the validity of Eq. (4), we considered two typical cases and showed the results in Figs. 4(a) and 4(b), respectively. The results calculated by using the MST [Eq. (2)] and RTOF [Eq. (4)] are shown by the blue solid lines and red circles, respectively. Clearly, these two results agree excellently well with each other, verifying the validity of Eq. (4). In Figs. 4(c) and 4(d), we also plotted the corresponding phase responses. Clearly, $\phi(x, y) = \phi(x + a, y)$ is indeed periodic and even symmetric with respect to the lines $x = Na$ and $x = (N + 1/2)a$.

Since $F_x(Na, y) = F_x(Na + a/2, y) \equiv 0$, we can find the equilibriums on the xy plane by just searching $F_y = 0$ along the high-symmetry lines $x = Na$ and $x = (N + 1/2)a$. However, the particle can be trapped only when the equilibrium is stable. The stability of the equilibrium can be determined by studying the eigenvalues of the force constant matrix around the equilibrium [54],

$$\vec{K} = \begin{pmatrix} \frac{\partial F_x}{\partial x} & \frac{\partial F_x}{\partial y} \\ \frac{\partial F_y}{\partial x} & \frac{\partial F_y}{\partial y} \end{pmatrix}, \quad (7)$$

where the matrix elements $\partial F_i / \partial r_j$ are numerically obtained by using the finite-difference method. For example, $\partial F_x / \partial x = \lim_{\Delta x} [F_x(x_0 + \Delta x, y_0) - F_x(x_0, y_0)] / \Delta x$, where (x_0, y_0) is the coordinate of the equilibrium and Δx is the longitudinal displacement of the particle from the equilibrium. Ignoring the ambient damping, the equilibrium is stable only when both eigenvalues of \vec{K} are purely real and negative [55].

In Fig. 5, we showed the stable equilibrium positions of dielectric cylinders with different radii and refractive indices. In Figs. 5(a) and 5(b), the radii of the cylinders are fixed while their refractive indices vary from 1 to 5. In contrast, the refractive indices of the cylinders in Figs. 5(c) and 5(d) are fixed while their radii change. The blue circles denote that the cylinder is stably trapped at $x = Na$, while the orange hexagons indicate that the cylinder is stably trapped at $x = (N + 1/2)a$. As a typical example, the eigenvalues of \vec{K} for the equilibriums indicated in Fig. 5(d) are plotted in Fig. 6. All the eigenvalues are real and negative, indicating the equilibriums are indeed stable.

In most cases, the cylinder can be trapped either at $x = Na$ or $x = (N + 1/2)a$. However, for some special cases, e.g., when the refractive index is $n = 1.5$ and the radius varies from $0.27a \sim 0.3a$, the cylinder can be captured at both sets

of positions. Also, the cylinders are likely trapped at $y < 0$. This is because when the radius and the refractive index of the cylinder are relatively small so that the scattering is not so significant, the optical force is dominant by the optical gradient force which tends to confine the cylinder at the positions where the electromagnetic fields are strong. From Figs. 5(e) and 5(f), we see that the strong electromagnetic fields are located at $y < 0$. In Figs. 3(c) and 3(d), we depicted the divergence and curl of the optical forces, where the parameters of the cylinder are $r = 0.12a$ and $n = 2.0$. The enlarged view of the rectangle region (marked by the dotted lines) containing the equilibrium position (stars) is plotted in Figs. 3(e) and 3(f). Clearly, the divergence of the force near the equilibrium position domains indicates that the optical force is dominant by the optical gradient force [56].

As can be seen from Figs. 5(b) and 5(c), the cylinder cannot be trapped solely by the optical force when the refractive index is too high or the radius is too large. However, since the longitudinal optical force oscillates between positive and negative, there is at least one stable longitudinal equilibrium ($F_x = 0$, $\partial F_x / \partial x < 0$) for any y when x varies a lattice period. As such, even though the cylinder cannot be trapped solely by the optical force, it will move upward or downward consistently and be finally confined with the help of both the optical force and the elastic force of the plate as it reaches the plate.

C. Self-assembly of cylinders

Since there is no mode conversion (including the backward surface mode), the chiral surface wave can bypass the obstacles without backscattering and restore to its original states after propagating a distance. Consequently, when a second cylinder is located far enough behind the first one, there will be no electromagnetic coupling from the first cylinder to the second one. On the other hand, because the chiral surface wave is immune to the backscattering, there will also be no electromagnetic coupling from the second cylinder to the first one. As a result, there is no optical binding force between the two cylinders, and they can be trapped by the chiral surface wave independently when they are separated far enough. Obviously, such analysis and conclusion can be applied to arbitrary number of cylinders which are separated far enough from each other.

Figure 7 depicts the optical forces acting on two identical cylinders. The cylinder on the left is fixed at the position where it can be stably trapped in the absence of the cylinder on the right. These two cylinders are located at the same y and separated by Na along the x direction, where N is an integer. Four pairs of identical cylinders are considered and their optical forces are plotted in different columns of Fig. 7. The longitudinal and transversal optical forces are shown in the upper and lower panels of Fig. 7, respectively. It is shown that for each pair of identical cylinders, they are subjected to almost the same transversal optical force. This indicates that the PCSW almost exerts no optical torque on the cylinder pairs. When the scattering cross sections of the cylinders are not so large, the cylinders can achieve stable equilibriums for the separation over $10a$; see Figs. 7(a)–7(c) and 6(e)–6(g). For the last pair of identical cylinders whose scattering cross sections are much larger, the separation

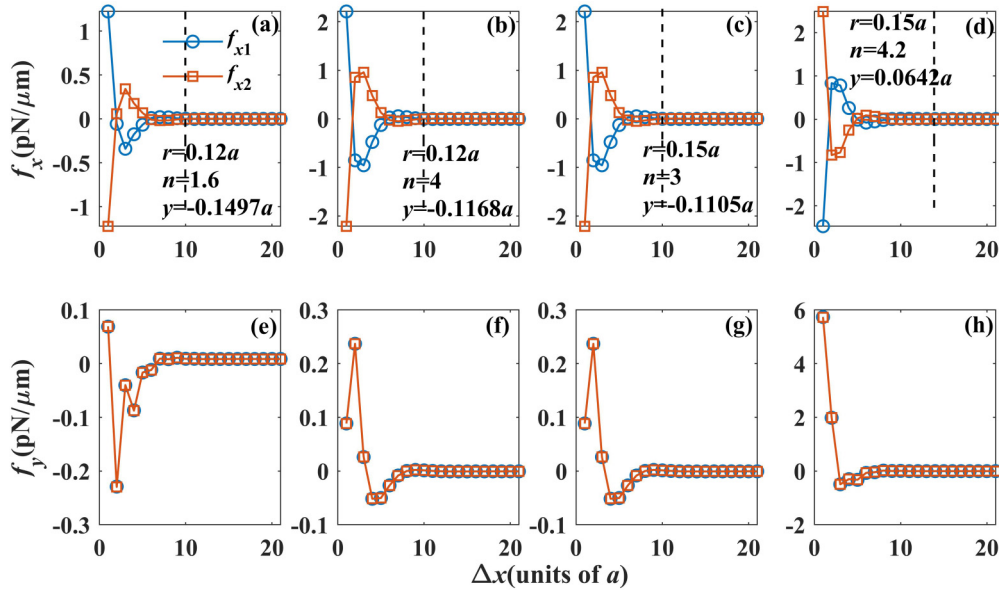


FIG. 7. The optical forces acting on two identical cylinders vs their separations. The blue circles (red squares) denote the optical forces acting on the left (right) cylinder. The longitudinal and transversal optical forces are shown in the upper and lower rows, respectively. In each column, the radii, refractive index, and y coordinates of the two cylinders are fixed. From left to right, $r = 0.12a$, $n = 1.6$, $y = -0.1497a$; $r = 0.12a$, $n = 4$, $y = -0.1168a$; $r = 0.15a$, $n = 3$, $y = -0.1105a$; and $r = 0.15a$, $n = 4.2$, $y = 0.0642a$. (The amplitude of the source was not given).

for achieving stable equilibriums has to be over $13a$; see Figs. 7(d) and 7(h).

Figure 8 depicts the optical forces acting on three identical cylinders. The parameters of the three cylinders are the same with those in Fig. 5(b). For the sake of convenience, locations of the first and the third cylinders are fixed and they are separated by $31a$, while the second cylinder in the middle of them is moved from left to right at an interval of the lattice constant a . In the same way, the fixed cylinders (the first and the third cylinders) are located at the positions where they can be stably trapped without the moving one, meanwhile all the cylinders are aligned in a line parallel to the x axis. Δx in Fig. 8 denotes the distance between the first and the second cylinder. It is shown that when $10a \leq \Delta x \leq 20a$, i.e., the distances between the adjacent cylinders are both not less than

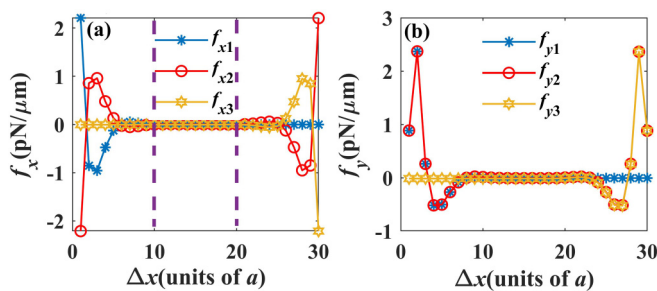


FIG. 8. The optical forces acting on three identical cylinders. (a) and (b) denote f_x and f_y , respectively. The first and the third cylinders are fixed with a separation between them of $30a$, while the second cylinder is in the middle of them and moved from left to right with a step of a . Δx denotes the distance between the first and the second cylinders. The parameters of the three cylinders are the same as those in Fig. 5(b).

$10a$, all three cylinders can reach the equilibriums. Because of the complexity of numerical calculation, we only showed the cases of two and three cylinders. However, in principle, we can trap arbitrary number of cylinders to realize self-assembly of cylinders into one-dimensional array by using the PCSW if the waveguide is long enough.

D. Trapping of cylinders of square and triangular shapes

Figure 9 shows the stable equilibrium positions of dielectric cylinders of square [Fig. 9(a)] and triangular [Fig. 9(b)] shapes as functions of refractive indices. The side lengths of the squares and equilateral triangles are both $0.2a$, and the refractive index ranges from 1.1 to 4. The blue circles denote that the particles are stably trapped at $x = Na$, while the orange hexagons indicate that the particles are stably trapped at $x = (N + 1/2)a$.

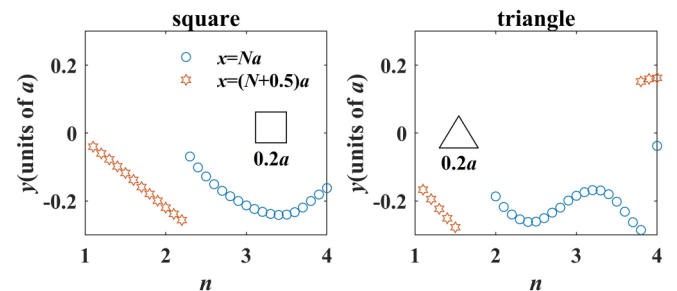


FIG. 9. The stable equilibrium positions of dielectric cylinders with square and triangular shapes as functions of refractive index. The side lengths of the squares and equilateral triangles are both $0.2a$.

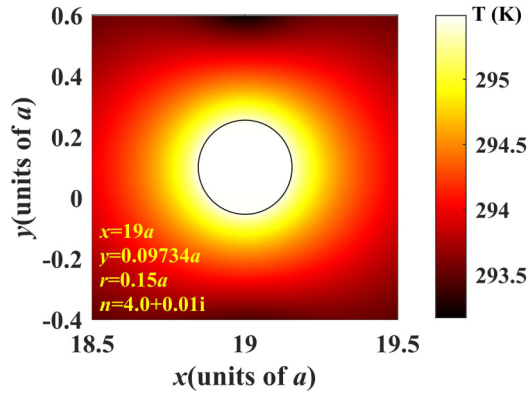


FIG. 10. Temperature distribution near the cylinder.

E. Photophoretic force

We also investigate the force induced by the light-induced thermal effect, i.e., the photophoretic force. For a typical example, here we assume the real part and imaginary part of the refractive index of the dielectric cylinder in the waveguide is 4 and 0.01, respectively. Because, the losses of dielectrics are usually negligible, the imaginary part of the dielectric cylinder is overestimated. The radius is $0.15a$. We first calculate the electric field distribution using the software COMSOL MULTIPHYSICS where the particle is located at the equilibrium position ($x = 20a$, $y = 0.09734a$). Then, the heat power volume density Q can be calculated as [57]

$$Q = \frac{1}{2} \varepsilon_0 \omega |\mathbf{E}|^2 \text{Im}[\varepsilon_r], \quad (8)$$

where ε_0 is the permittivity in free space, ω is angular frequency of the PCSW, \mathbf{E} denotes the electric fields, $\text{Im}[\]$ denotes the imaginary part of $\[\]$, ε_r is the relative permittivity of the particle. The heat power volume density Q is considered as the heat source in the thermal transfer problem solved by COMSOL. The heat conductivity of air and the cylinder in the waveguide are $k_a = 0.04 \text{ WK}^{-1} \text{ m}^{-1}$ and $k_p = 2 \text{ WK}^{-1} \text{ m}^{-1}$, respectively. The temperature distribution is plotted in Fig. 10.

The photophoretic force acting on the cylinder is computed as [58–60]

$$F_{x(y)}^{\text{PPF}} = -\frac{15k_B\alpha}{64\sqrt{2}\sigma_{\text{cs}}} \frac{dT}{dx(y)}, \quad (9)$$

where $k_B = 1.38 \times 10^{-23} \text{ J K}^{-1}$ is Boltzmann constant; $\sigma_{\text{cs}} = 4.3 \times 10^{-19} \text{ m}^2$ is the scattering cross section of air molecules at 1 atm and the room temperature. The thermal accommodation coefficient α at $T = 300 \text{ K}$ is about 0.8–0.9; here, we take $\alpha = 0.8$. $\frac{dT}{dx} = \frac{T(x=19.15a) - T(x=18.85a)}{2r}$ and $\frac{dT}{dy} = \frac{T(y=0.2473a) - T(y=-0.0527a)}{2r}$ are the temperature gradient across the particle with r being the radius of the cylinder; l is the size of the particle parallel to the temperature gradient of the particle. According to Eq. (9), the calculated photophoretic forces at the equilibrium position are $F_x^{\text{PPF}} = 2.6 \times 10^{-6} \text{ pN}/\mu\text{m}$ and $F_y^{\text{PPF}} = -3.5 \times 10^{-3} \text{ pN}/\mu\text{m}$, respectively, which are several orders weaker than the optical force (about $1 \text{ pN}/\mu\text{m}$) which can be ignored compared with the optical force of the nonequilibrium positions. As a consequence, the thermal effect could be neglected in the optical trapping.

III. CONCLUSIONS

In summary, we show the stable trapping and self-assembly of particles of arbitrary sizes, shapes, and dielectric constants can be achieved by PCSWs. The achievement of the stable trapping and self-assembly is due to the fact that the PCSW can navigate the particles and restore to its original state. Although the chiral surface wave is propagating, the trapping and self-assembly are static, which is in stark contrast to those of using freely propagating beams [39–41] and topologically trivial surface waves where trapping and self-assembly are dynamic. Due to the novel transporting and scattering properties, topologically nontrivial surface waves including the PCSWs, photonic helical surface waves, and valley-polarized surface waves have great prospects in optical manipulation applications. Our work paves the way for optical trapping and self-assembly based on topological nontrivial surface waves.

ACKNOWLEDGMENTS

The authors acknowledge the support of the National Science Foundation of China (Grants No. 12104069, No. 12174263, and No. 1904237), the Open Research Fund of Hunan Provincial Key Laboratory of Flexible Electronic Materials Genome Engineering through Grant No. 202007, the Scientific Research Foundation of Hunan Provincial Education Department through Grant No. 19C0034, the National Natural Science Foundation of Hunan Province (Grant No. 2021JJ40554), and Natural Science Foundation of Guangdong Province (Grant No. 2020A1515010669).

APPENDIX: SYMMETRY OF THE PHASE RESPONSE

In this Appendix, we will show that for a circular cylinder, the phase response as a function of the cylinder's location possesses the even symmetry about the high-symmetry lines of the unit cell. For example, for the high-symmetry line $x = Na$, where N is an integer, the phase response is identical for the cylinder located at the original position (gray disk) and for the cylinder located at its mirror-reflection position (dashed circle) as shown in Fig. 11(a).

We first demonstrate the equivalence of the phase responses between system 1 shown in Fig. 11(b) and system 2 shown in Fig. 11(c). The source and monitor points of system 1 (2) are marked by A (B) and B (A) in Fig. 11(a), respectively. Interchanging the source and monitor points and reversing the sign of the biased magnetic field (transposing the permeability tensor) of system 1, system 2 is obtained. According to the Lorentz reciprocal theorem [61–63], the input and output of the two systems are equivalent. As such, the phase responses of the two systems detected are equal, $\varphi^1 = \varphi^2$. Then, we rotate system 2 with respect to the high-symmetry line (the purple dashed line) 180° to obtain system 3 as shown in Fig. 11(d). Note that the rotation turns system 2 upside down. Thus, the directions of biased magnetic fields in system 2 and system 3 are opposite. The equivalence between system 2 and system 3 leads to the identity of the phase responses, $\varphi^2 = \varphi^3$. As a consequence, $\varphi^1 = \varphi^3$. Also, system 3 can be obtained by just moving the circular cylinder in system 1 to its mirror-reflection position respect to the high system line. Therefore, the phase responses are the same when the circular

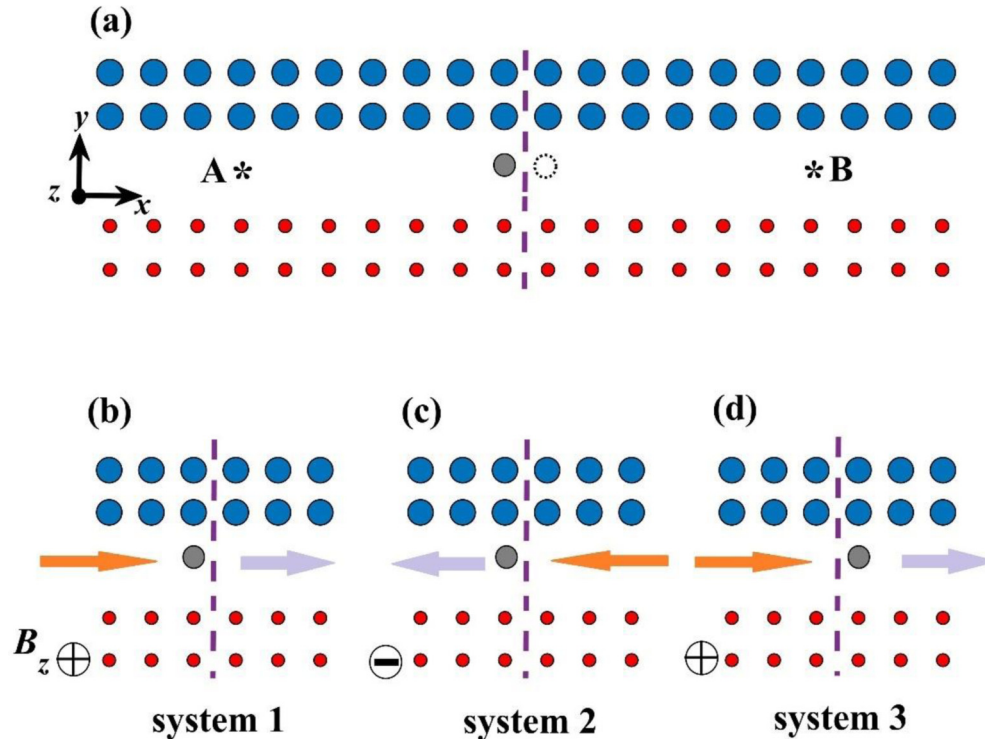


FIG. 11. (a) Schematics of the structure with the particle at its original position (gray disk) and the mirror-reflected position (dashed circle). The operations are conducted in two steps: from the original system (b) to its reciprocal pair (c), and to (e) the system after a mirror operation. “+” and “-” signs represent the direction of the biased magnetic field along z direction.

cylinder is moved to its mirror-reflection position, indicating that the phase response $\varphi(x, y)$ possesses even symmetry with

respect to the high-symmetry lines $x = Na$. Similarly, it is true for high-symmetry lines $x = (N + 1/2)a$.

- [1] A. Ashkin, *Phys. Rev. Lett.* **24**, 156 (1970).
- [2] A. Ashkin, J. M. Dziedzic, J. E. Bjorkholm, and S. Chu, *Opt. Lett.* **11**, 288 (1986).
- [3] W. Ding, T. Zhu, L. Zhou, and C. Qiu, *Adv. Photonics* **1**, 024001 (2019).
- [4] S. Chu, *Rev. Mod. Phys.* **70**, 685 (1998).
- [5] C. N. Cohen-Tannoudji, *Rev. Mod. Phys.* **70**, 707 (1998).
- [6] S. Giorgini, L. P. Pitaevskii, and S. Stringari, *Rev. Mod. Phys.* **80**, 1215 (2008).
- [7] A. D. Mehta, M. Rief, J. A. Spudich, D. A. Smith, and R. M. Simmons, *Science* **283**, 1689 (1999).
- [8] S. Stoll, J. Delon, T. M. Brotz, and R. N. Germain, *Science* **296**, 1873 (2002).
- [9] Q. Zhao, H. W. Wang, P. P. Yu, S. H. Zhang, J. H. Zhou, Y. M. Li, and L. Gong, *Front. Bioeng. Biotechnol.* **8**, 422 (2020).
- [10] J. Zhou, A. I. Chizhik, S. Chu, and D. Jin, *Nature (London)* **579**, 41 (2020).
- [11] O. Romero-Isart, A. C. Pflanzer, F. Blaser, R. Kaltenbaek, N. Kiesel, M. Aspelmeyer, and J. I. Cirac, *Phys. Rev. Lett.* **107**, 020405 (2011).
- [12] Y. Yang, Y. Ren, M. Chen, Y. Arita, and C. Rosales-Guzmán, *Adv. Photonics* **3**, 034001 (2021).
- [13] Y. Zhang, J. Shen, Z. Xie, X. Dou, C. Min, T. Lei, J. Liu, S. Zhu, and X. Yuan, *Nanoscale* **9**, 10694 (2017).
- [14] X. Y. Wang, Y. M. Dai, Y. Q. Zhang, C. J. Min, and X. C. Yuan, *ACS Photonics* **5**, 2945 (2018).
- [15] Y. Q. Zhang, C. J. Min, X. Dou, X. Wang, H. P. Urbach, M. G. Somekh, and X. C. Yuan, *Light Sci. Appl.* **10**, 59 (2021).
- [16] P. R. Huft, J. D. Kolbow, J. T. Thweatt, and N. C. Lindquist, *Nano Lett.* **17**, 7920 (2017).
- [17] D. Ganic, X. Gan, and M. Gu, *Opt. Express* **12**, 5533 (2004).
- [18] L. Kong, C. Lee, C. M. Earhart, B. Cordovez, and J. W. Chan, *Opt. Express* **23**, 6793 (2015).
- [19] Y. F. Xiang, X. Tang, C. J. Min, G. H. Rui, Y. Kuai, F. Y. Lu, P. Wang, H. Ming, Q. W. Zhan, X. C. Yuan, J. R. Lakowicz, and D. G. Zhang, *Ann. Phys.* **532**, 1900497 (2020).
- [20] N. Wang, R.-Y. Zhang, and C. T. Chan, *Opt. Express* **29**, 20590 (2021).
- [21] Y. Q. Zhang, J. Wang, J. F. Shen, Z. S. Man, W. Shi, C. J. Min, G. H. Yuan, S. W. Zhu, H. P. Urbach, and X. C. Yuan, *Nano Lett.* **14**, 6430 (2014).
- [22] Y. Q. Zhang, W. Shi, Z. Shen, Z. S. Man, C. J. Min, J. F. Shen, S. W. Zhu, H. P. Urbach, and X. C. Yuan, *Sci. Rep.* **5**, 15446 (2015).
- [23] C. J. Min, Z. Shen, J. F. Shen, Y. Q. Zhang, H. Fang, G. H. Yuan, L. P. Du, S. W. Zhu, T. Lei, and X. C. Yuan, *Nat. Commun.* **4**, 2891 (2013).
- [24] Y. Xiang, X. Tang, Y. Fu, F. Lu, Y. Kuai, C. Min, J. Chen, P. Wang, J. R. Lakowicz, X. Yuan, and D. Zhang, *Nanoscale* **12**, 1688 (2020).
- [25] N. Wang, R. Y. Zhang, and C. T. Chan, *Phy. Rev. Appl.* **15**, 024034 (2021).

- [26] C. Zhan, G. Wang, J. Yi, J. Wei, Z. Li, Z. Chen, J. Shi, Y. Yang, W. Hong, and Z. Tian, *Matter* **3**, 1350 (2020).
- [27] S. J. Yoon, J. Lee, S. Han, C. K. Kim, C. W. Ahn, M. K. Kim, and Y. H. Lee, *Nat. Commun.* **9**, 2218 (2018).
- [28] M. Belkin, S. H. Chao, M. P. Jonsson, C. Dekker, and A. Aksimentiev, *ACS Nano* **9**, 10598 (2015).
- [29] D. V. Verschueren, S. Pud, X. Shi, L. De Angelis, L. Kuipers, and C. Dekker, *ACS Nano* **13**, 61 (2019).
- [30] T. T. Zhu, Y. Y. Cao, L. Wang, Z. Q. Nie, T. Cao, F. K. Sun, Z. H. Jiang, M. Nieto-Vesperinas, Y. M. Liu, C. W. Qiu, and W. Q. Ding, *Phys. Rev. Lett.* **120**, 123901 (2018).
- [31] H. Li, Y. Y. Cao, B. J. Shi, T. Zhu, Y. Geng, R. Feng, L. Wang, F. Sun, Y. Shi, M. A. Miri, M. Nieto-Vesperinas, C.-W. Qiu, and W. Ding, *Phys. Rev. Lett.* **124**, 143901 (2020).
- [32] H. Li, Y. Y. Cao, L. M. Zhou, X. X. Xu, T. T. Zhu, Y. Z. Shi, C. W. Qiu, and W. Q. Ding, *Adv. Opt. Photonics* **12**, 288 (2020).
- [33] R. C. Jin, Y. H. Xu, Z. G. Dong, and Y. M. Liu, *Nano Lett.* **21**, 10431 (2021).
- [34] T. T. Zhu, A. Novitsky, Y. Y. Cao, M. R. C. Mahdy, L. Wang, F. K. Sun, Z. H. Jiang, and W. Q. Ding, *Appl. Phys. Lett.* **111**, 061105 (2017).
- [35] L. F. Yang and K. J. Webb, *Phys. Rev. B* **103**, 245124 (2021).
- [36] N. Wang, R. Y. Zhang, Q. H. Guo, S. B. Wang, G. P. Wang, and C. T. Chan, *Phys. Rev. B* **105**, 014104 (2022).
- [37] D. L. Gao, W. Q. Ding, M. Nieto-Vesperinas, X. M. Ding, M. Rahman, T. H. Zhang, C. T. Lim, and C. W. Qiu, *Light Sci. Appl.* **6**, e17039 (2017).
- [38] M. M. Burns, J. M. Fournier, and J. A. Golovchenko, *Phys. Rev. Lett.* **63**, 1233 (1989).
- [39] L. Y. Cui, X. Li, J. Chen, Y. Y. Cao, G. Q. Du, and J. Ng, *Phys. Rev. A* **96**, 023833 (2017).
- [40] L. Y. Cui, G. Q. Du, and J. Ng, *Phys. Rev. A* **102**, 023502 (2020).
- [41] L. Y. Cui and H. Yin, *New J. Phys.* **23**, 073037 (2021).
- [42] Z. Wang, Y. D. Chong, J. D. Joannopoulos, and M. Soljacic, *Phys. Rev. Lett.* **100**, 013905 (2008).
- [43] Z. Wang, Y. D. Chong, J. D. Joannopoulos, and M. Soljacic, *Nature (London)* **461**, 772 (2009).
- [44] P. Rakich, M. A. Popovic, and Z. Wang, *Opt. Express* **17**, 18116 (2009).
- [45] Z. Wang and P. Rakich, *Opt. Express* **19**, 22322 (2011).
- [46] D. M. Pozar, *Microwave Engineering* (Wiley, New York, 1998).
- [47] C. Hermann, V. A. Kosobukin, G. Lampel, J. Peretti, V. I. Safarov, and P. Bertrand, *Phys. Rev. B* **64**, 235422 (2001).
- [48] J. B. González-Díaz, A. García-Martín, G. Armelles, J. M. García-Martín, C. Clavero, A. Cebollada, R. A. Lukaszew, J. R. Skuza, D. P. Kumah, and R. Clarke, *Phys. Rev. B* **76**, 153402 (2007).
- [49] M. V. Sapozhnikov, S. A. Gusev, B. B. Troitskii, and L. V. Khokhlova, *Opt. Lett.* **36**, 4197 (2011).
- [50] J. C. Banthí, D. Meneses-Rodríguez, F. García, M. U. González, A. García-Martín, A. Cebollada, and G. Armelles, *Adv. Mater.* **24**, OP36 (2012).
- [51] L. Lu, J. D. Joannopoulos, and M. Soljacic, *Nature Photonics* **8**, 821 (2014).
- [52] L. Y. Cui, N. Wang, and J. Ng, *Phys. Rev. A* **104**, 013508 (2021).
- [53] D. L. Wang, Ph.D. thesis and dissertation, The University of Texas at Austin, 2018.
- [54] J. Ng, Z. F. Lin, C. T. Chan, and P. Sheng, *Phys. Rev. B* **72**, 085130 (2005).
- [55] J. Ng, Z. F. Lin, and C. T. Chan, *Phys. Rev. Lett.* **104**, 103601 (2010).
- [56] J. J. Du, C.-H. Yuen, X. Li, K. Ding, G. Q. Du, Z. F. Lin, C. T. Chan, and J. Ng, *Sci. Rep.* **7**, 18042 (2017).
- [57] X. Chen, Y. T. Chen, M. Yan, and M. Qiu, *ACS Nano* **6**, 2550 (2012).
- [58] M. Scandurra, F. Iacopetti, and P. Colona, *Phys. Rev. E* **75**, 026308 (2007).
- [59] J. S. Lu, H. B. Yang, L. N. Zhou, Y. Q. Yang, S. Luo, Q. Li, and M. Qiu, *Phys. Rev. Lett.* **118**, 043601 (2017).
- [60] L. H. Lin, M. S. Wang, X. L. Peng, E. N. Lissek, Z. M. Mao, L. Scarabelli, E. Adkins, S. Coskun, H. E. Unalan, B. A. Korgel, L. M. Liz-Marzan, E. L. Florin, and Y. B. Zheng, *Nature Photonics* **12**, 195 (2018).
- [61] C.-T. Tai, *IEEE Trans. Antenn. Propag.* **40**, 675 (1992).
- [62] D. Pisssoort and F. Olyslager, *IEEE T. Microw. Theory* **52**, 542 (2004).
- [63] A. T. De Hoop, *Appl. Sci. Res.* **8**, 135 (1960).